Nanotechnology **21** (2010) 255503 (8pp) doi:10.1088/0957-4484/21/25/255503

A single molecule immunoassay by localized surface plasmon resonance

Kathryn M Mayer[1,2], Feng Hao[1,2], Seunghyun Lee[2,3], Peter Nordlander[1,2] and Jason H Hafner[1,2,3]

[1] Department of Physics and Astronomy, Rice University, 6100 Main Street, Houston, TX, USA
[2] Laboratory for Nanophotonics, Rice University, 6100 Main Street, Houston, TX, USA
[3] Department of Chemistry, Rice University, 6100 Main Street, Houston, TX, USA

Received 31 January 2010, in final form 10 May 2010
Published 2 June 2010
Online at stacks.iop.org/Nano/21/255503

Abstract
Noble metal nanoparticles exhibit sharp spectral extinction peaks at visible and near-infrared frequencies due to the resonant excitation of their free electrons, termed localized surface plasmon resonance (LSPR). Since the resonant frequency is dependent on the refractive index of the nanoparticle surroundings, LSPR can be the basis for sensing molecular interactions near the nanoparticle surface. However, previous studies have not yet determined whether the LSPR mechanism can reach the ultimate sensing limit: the detection of individual molecules. Here we demonstrate single molecule LSPR detection by monitoring antibody–antigen unbinding events through the scattering spectra of individual gold bipyramids. Both experiments and finite element simulations indicate that the unbinding of single antigen molecules results in small, discrete <0.5 nm blue-shifts of the plasmon resonance. The unbinding rate is consistent with antibody–antigen binding kinetics determined from previous ensemble experiments. According to these results, the effective refractive index of a single protein is approximately 1.54. LSPR sensing could therefore be a powerful addition to the current toolbox of single molecule detection methods since it probes interactions on long timescales and under relatively natural conditions.

1. Introduction

Noble metal nanoparticles exhibit sharp spectral extinction peaks at visible and near-infrared frequencies due to the resonant excitation of their free electrons; this phenomenon is termed localized surface plasmon resonance (LSPR). Since the resonant frequency is dependent on the refractive index of the nanoparticle's surroundings, LSPR can be the basis for sensing molecular interactions near the nanoparticle surface [1]. However, previous studies have not yet determined whether the LSPR mechanism can reach the ultimate sensing limit: the detection of individual molecules [2–4]. From a qualitative point of view, it is plausible that the scattering spectra from single plasmon resonant nanoparticles could transduce single molecule events. Elongated gold and silver nanoparticles can have high refractive index sensitivities that are localized to nanometre-scale sensing volumes surrounding sharp tips [5, 6]. If a single macromolecule such as a protein with a refractive index different from water enters or leaves this sensing volume, one would expect a discernible shift in the peak wavelength of the plasmon resonance. Here we demonstrate single molecule LSPR detection by monitoring antibody–antigen unbinding events through the scattering spectra of individual gold bipyramids [7]. The unbinding rate is consistent with antibody–antigen binding kinetics determined from previous ensemble experiments [8, 9]. LSPR sensing could therefore be a powerful addition to the current toolbox of single molecule detection methods since it probes interactions on long timescales and under relatively natural conditions.

2. Methods

2.1. Bipyramid synthesis

All solutions were prepared freshly for each synthesis using deionized (DI) water, except for the hydrogen tetrachloroaurate(III) (Sigma, No. 520918), which was prepared as a 28 mM stock solution from a dry ampoule and stored in the dark. First, sodium citrate-stabilized

gold seed particles were prepared. A 20 ml solution of 0.125 mM hydrogen tetrachloroaurate(III) and 0.25 mM sodium citrate (Fisher, No. S279) was prepared and mixed briefly. Next, 0.3 ml of 10 mM $NaBH_4$ (Acros, No. 18930) solution prepared at room temperature was added, followed by mixing for 2 min. The resulting gold seed solution was kept at room temperature for at least 2 h for complete reaction, after which it appeared dark pink. Next, 0.5 ml of 10 mM hydrogen tetrachloroaurate(III) and 10 ml of 100 mM cetyltrimethylammonium bromide (CTAB) (Sigma, No. H9151) were mixed with 0.1 ml of 10 mM silver nitrate (Acros, No. 19768) for the growth solution. Then, 0.2 ml of 1.0 M hydrochloric acid (Hampton Research, No. HR2-581) and 0.08 ml of 100 mM L-ascorbic acid (Fisher, No. A61) were added to the solution in order. Finally, 20 μl of the seed solution was added to the growth solution. The solution was kept at 28 °C for several hours. During this time, the colour changed gradually from almost clear to dark pink, with most of the colour change occurring in the first hour.

2.2. Atomic force microscopy (AFM) characterization of bipyramids

Bipyramids were deposited onto a glass cover slip by the previously described method of PEGylation and exposure to an APTES functionalized glass cover slip, followed by plasma cleaning [9]. AFM was carried out in tapping mode using a Veeco Nanoscope IV with a scan size of 4 μm and scan rate of 1 Hz.

2.3. Single particle optical measurements

Optical images and spectra were collected using a Zeiss Axiovert 200 microscope in an epi-illumination, dark field scattering configuration, with a magnification of 50× and numerical aperture of 0.5. Images were collected using a thermoelectrically cooled CCD camera (Roper PhotonMax). Single particle spectra were obtained by using a micromanipulation stage to align the particle with a slit located in a confocal imaging plane. The scattered light from the selected particle was analysed using an Acton SpectraPro spectrograph and the aforementioned camera. Spectra were collected with integration times of 30–60 s.

2.4. Spectral analysis

Spectra were collected by the CCD camera in the form of spectrograph images of 512 pixels × 512 pixels, in which the horizontal axis represents the particle's position in the slit, and the vertical axis represents wavelength. The wavelength scale was calibrated using a standard filter set. To account for the variation of detector efficiency with wavelength, a white calibration was carried out on a reflection standard (Edmund Optics). A MATLAB program was developed to analyse the spectral images by summing the intensity at each wavelength within a few pixels of the particle, and subtracting the background intensity. Each resulting spectrum was fit with a Gaussian, and the resulting peak wavelengths were plotted versus time.

2.5. Single particle immunoassay

To prepare a sparse film of particles, 40 μl of bipyramid solution was drop-cast onto a piranha-cleaned glass cover slip. (Warning: piranha solution is very reactive and corrosive; use extreme caution!) The cover slip was then rinsed with copious amounts of DI water to remove CTAB. A flow cell was then assembled consisting of a 1 mm thick PDMS layer sandwiched between two layers of glass. The bottom glass layer (closest to the microscope objective) was the aforementioned cover slip with gold bipyramids deposited on the top side. The PDMS layer had a cut-out of approximately 2 mm × 10 mm in the centre, creating a flow volume of about 20 μl. The top glass layer was a standard microscope slide, with two drilled holes sealed to syringe needles that served as the flow inlet and outlet. The entire assembly was placed on the microscope stage, and the particles were imaged through the bottommost cover slip. The flow system was regulated by a syringe pump on the outlet side of the flow cell, withdrawing liquid at a constant rate of 100 μl min^{-1}. Solutions entered from a set of reservoirs connected by a six-way valve to the flow cell. All components were connected with silicone tubing. The flow system was flushed through with buffer before each experiment to purge any air bubbles. In the immunoassay experiments, MES buffer (2-(*N*-morpholino)ethanesulfonic acid, 0.1 M) at pH 6.1 was first flowed over the substrate for at least 30 min. Next, the capture antibody, Rabbit IgG, was flowed over the substrate for at least 30 min at 300 μg ml^{-1} in MES buffer. Then, the substrate was rinsed with MES buffer for another 30 min to remove any excess capture antibody. Next, the target antibody, Goat anti-Rabbit IgG, was flowed over the substrate for at least 1 h at 10 nM in PBS (phosphate buffered saline, 0.05 M with 0.15 M NaCl) at pH 7.6. Finally, the substrate was rinsed for at least 8 h in PBS.

3. Results and discussions

Single gold bipyramids in the form of ten-sided polyhedra were chosen as the sensors for these experiments [7]. As synthesized here, they are approximately 140 nm long and 50 nm wide, and are monodisperse in terms of size and shape (figure 1(a)). The bipyramids have sharp tips and are highly sensitive to the surrounding refractive index, with a figure of merit (FOM, defined as the refractive index sensitivity divided by the plasmon resonance line width) greater than four [9, 10]. Gold nanospheres are also present in the sample, but the bipyramids and nanospheres have distinct plasmon resonances as seen in their ensemble spectral extinction (figure 1(b)). When the particles were deposited on a substrate and imaged by dark field microscopy, only the nanospheres were clearly visible to the eye since the bipyramid scattering is peaked at 875 nm. To illustrate how the particle types were differentiated, figures 1(d) and (e) present two dark field optical images of a nanosphere (left) and a bipyramid (right), one taken by a colour camera (d), where the nanosphere appears bright green and the bipyramid is extremely faint, and one taken by a near-infrared CCD (e), where the bipyramid appears much brighter. Scattering spectra of individual nanoparticles were recorded

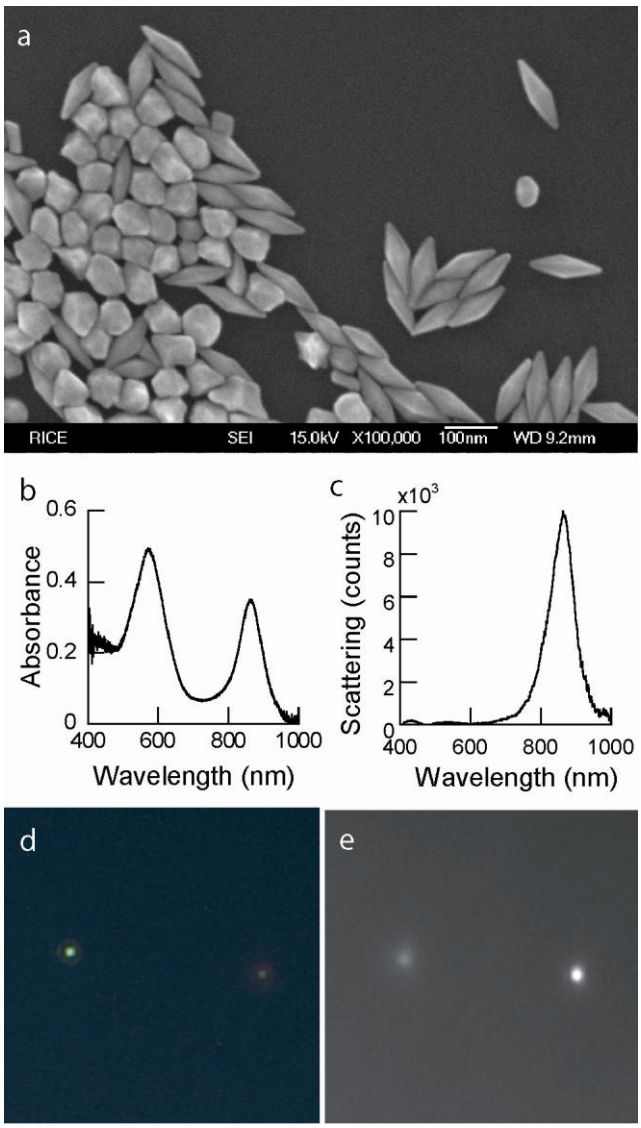

Figure 1. Gold bipyramids. (a) SEM image showing the bipyramids' structure. (b) Ensemble extinction measurement, showing the LSPR of nanospheres (580 nm) and bipyramids (875 nm). (c) Typical scattering spectrum of a single bipyramid. (d) Dark field scattering images of a nanosphere (left) and a bipyramid (right) captured with a colour camera and (e) captured with a CCD that is sensitive into the near-infrared.

with an imaging spectrograph attached to the microscope. Figure 1(c) displays a single bipyramid's scattering spectrum collected with a 30 s integration time. Note that the spectral peak is intense and relatively narrow, since the peak is in the near-infrared region where gold is minimally absorptive [11].

In addition to the aforementioned favourable optical properties, the structure of the bipyramid and its orientation on the substrate enhance its sensing capabilities. Due to their facetted structure, bipyramids sit on the substrate with one tip elevated and exposed to the solution. This can be seen in the uneven contrast of the isolated bipyramids in figure 1(a), and is shown more definitively by AFM. Figure 2(a) displays the topography of the bipyramid sample with a 90 nm linear grey scale. The AFM images show uneven contrast in the topographic image of isolated bipyramids. Figure 2(b) displays the same image with a colour scale designed to highlight variations in topography. Here one can see that one end of the isolated bipyramids slopes down while the other is flat. Finally, an AFM cross section is presented in figures 2(c) and (d) that also supports the case that bipyramids sit on the substrate with one tip exposed to the solution. Because of this exposed sharp tip, the local refractive index of a molecular-scale volume in the solution can be monitored by tracking the LSPR peak of a single bipyramid. It is this extreme localization of the sensing volume, which is absent in nanoparticles of other shapes [4, 12–18] that makes the bipyramid a strong candidate particle for single molecule detection.

In the single particle immunoassay experiments described here, bipyramid spectra were recorded over a period of 12 h as the nanoparticle was exposed first to a capture antibody, then to a specific target molecule (a secondary antibody), and then rinsed with buffer (figure 3). In this data, shifts in the plasmon peak occur in response to local changes in the dielectric environment surrounding the bipyramid. In particular, red-shifts correspond to molecules binding to the particle surface, since the refractive index of protein is higher than that of buffer, and conversely, blue-shifts correspond to molecules unbinding from the surface. The LSPR peak wavelength shift versus time from a typical single particle immunoassay experiment is shown in figure 5(a). At point 1, the capture antibody (Rabbit IgG) was added and the spectrum red-shifted as antibodies coated the gold nanoparticle surface. At point 2 the target molecule (Goat anti-Rabbit IgG) was added and again the spectrum red-shifted, this time by a smaller amount since the target molecules are further from the bipyramid surface than the capture antibody. During these steps, our ∼30 s time resolution was not sufficient to capture discrete single molecule binding events within the fast association processes. At point 3 the sample was rinsed once again. During this final rinse single molecule events were detected as discrete blue-shifts in the LSPR peak wavelength due to the unbinding of single target molecules. We chose to study these single molecule unbinding events (as opposed to searching for discrete red-shifts as molecules bind to the nanoparticle), because the dissociation is slow enough that one can measure the rate to confirm it matches an established value [8, 9]. In this case, the expected rate of dissociation of the target from the capture antibody is 6.5×10^{-5} s^{-1} and, unlike the association rate, it should not be affected by the initial target concentration or any diffusion effects [8]. Thus, kinetics information can confirm that the observed events are indeed the antibody–antigen dissociation of interest.

Both the measurements displayed in figure 5(a) and the numerical simulations described below indicate that the LSPR peak shift due to single target molecule unbinding is only a few tenths of a nanometre, which is very close to the noise level (in this case the fluctuations in the measured LSPR peak wavelength). To analyse the data, we calculated the cross-correlation function (CCF) between the measurements and a test function consisting of a discrete blue-shift at every point in the time series. For the sequence of six data points starting

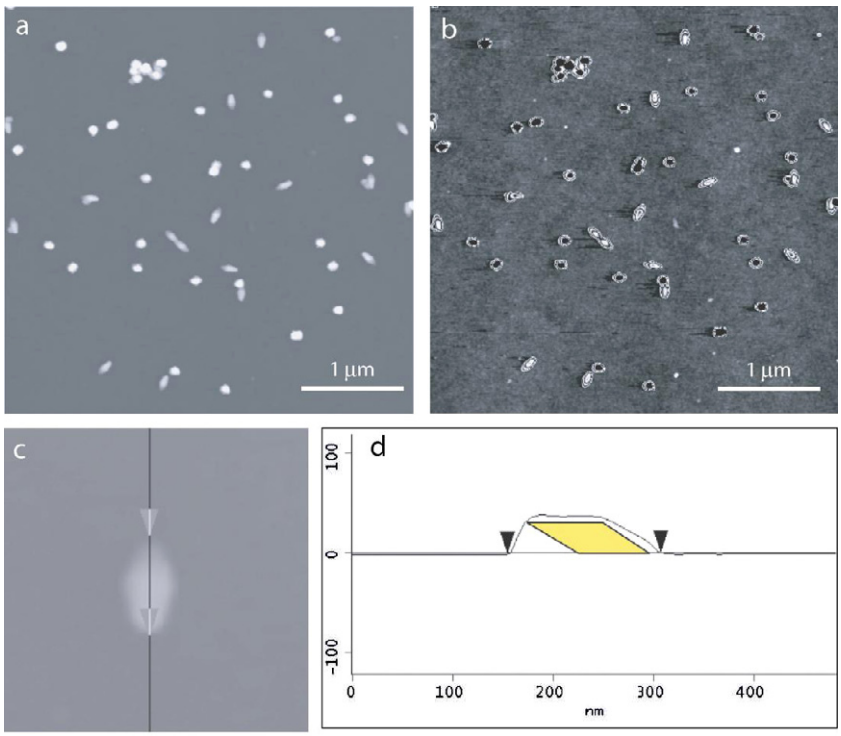

Figure 2. Bipyramid position on the substrate. (a) AFM of isolated gold bipyramids on a glass substrate with a linear grey scale. (b) The same image as in (a) but with a z-scale designed to highlight changes in height. (c) A zoom of one of the bipyramids in (a) with a line indicating a cross section. (d) The cross section drawn in (c) which demonstrates the position of the bipyramids as indicated.

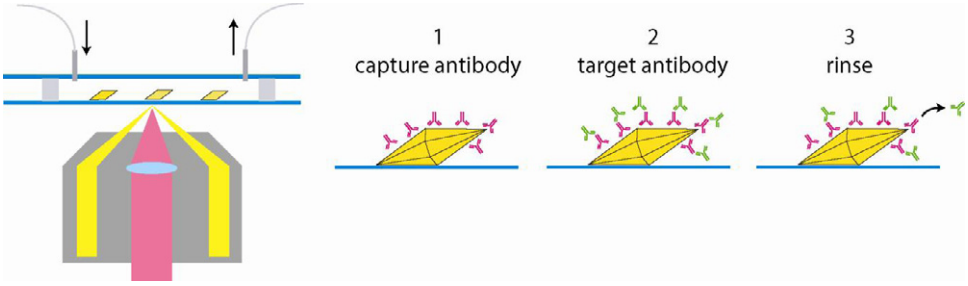

Figure 3. Schematic of the single particle immunoassay. The dark field microscopy setup with flow cell, and the (1) capture antibody binding, (2) target binding, and (3) rinsing steps of the assay.

with the ith time step, the CCF was calculated as:

$$\mathrm{CCF} = \frac{(\lambda_i + \lambda_{i+1} + \lambda_{i+2}) - (\lambda_{i+3} + \lambda_{i+4} + \lambda_{i+5})}{\sigma_1 + \sigma_2}.$$

The numerator takes the form of the dot product of the data with a step function having the values (1, 1, 1, −1, −1, −1). This quantity is maximized when the data include a discrete blue-shift between points $(i + 2)$ and $(i + 3)$, and minimized (i.e. CCF has a large negative value) when the data include a red-shift. CCF is calculated for $i = 1$ through $(N - 5)$, where N is the total length of the data series. In the denominator, σ_1 and σ_2 are the standard deviations in the data points i through $(i + 2)$, and $(i + 3)$ through $(i + 5)$, respectively. Dividing by this factor enhances our ability to detect single molecule events because it will favour those events consisting of a clear step with low noise on either side. (This factor also accounts for the final cross-correlation having a magnitude greater than one in some cases, since this is not a standard normalization.) Once CCF has been calculated for the entire data series, the ten time points with the largest CCF values are designated as likely single molecule events.

The process is then repeated with one small difference: the cross-correlation is calculated for groupings of seven data points rather than six, in order to pick up those events which did not occur near the beginning of one of the 30 s CCD exposures. As illustrated in figure 4(a), unbinding near the boundary between two exposures will produce the discrete shift described by the test function above. However, as illustrated in figure 4(b), unbinding near the middle of a frame will produce an intermediate peak wavelength since the frame will contain a sum of data from the blue and red peaks. For this

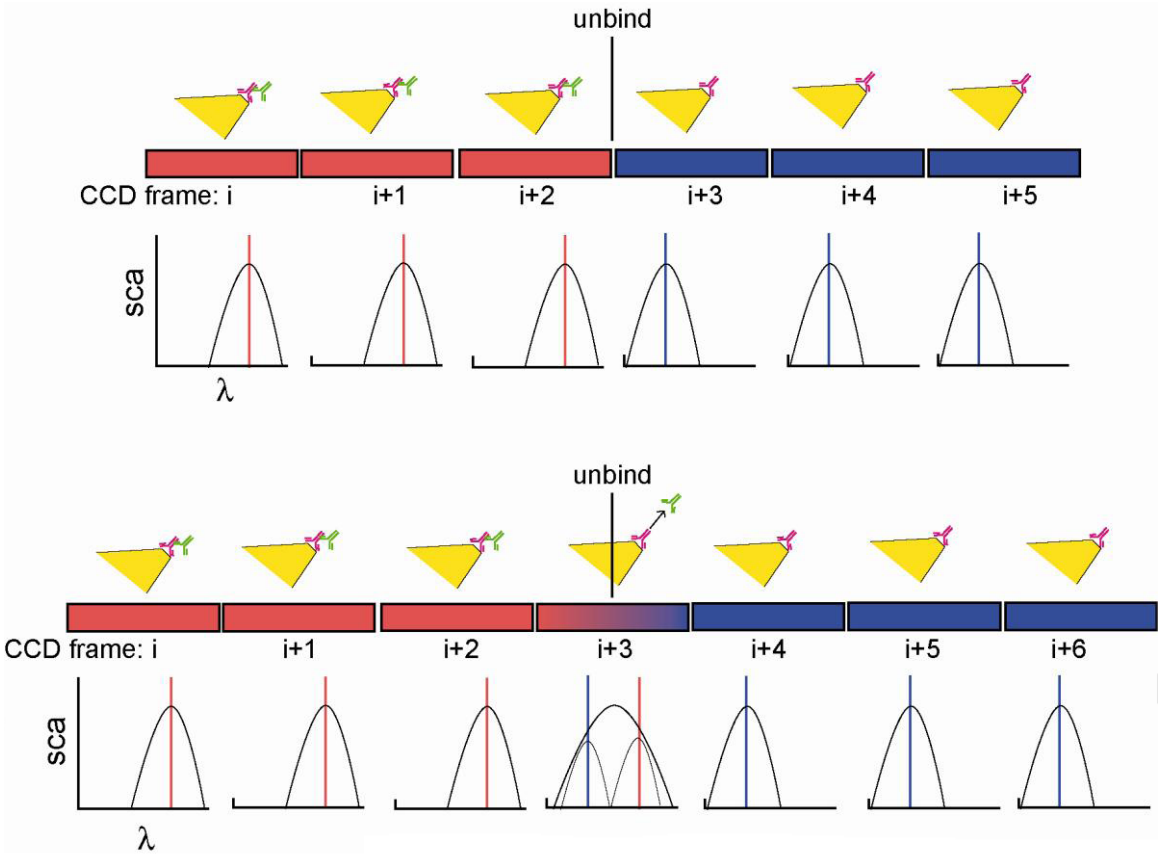

Figure 4. Schematic of unbinding event timing and detection. First row: when the molecule unbinds near the boundary of two frames, a discrete blue-shift is measured between frames $(i + 2)$ and $(i + 3)$. Second row: when the molecule unbinds in the middle of an integration time, the spectral peak is artificially broadened in that frame, so a discrete shift can only be measured between frames $(i + 2)$ and $(i + 4)$.

case, the cross-correlation is calculated as:

$$\mathrm{CCF} = \frac{(\lambda_i + \lambda_{i+1} + \lambda_{i+2}) - (\lambda_{i+4} + \lambda_{i+5} + \lambda_{i+6})}{\sigma_1 + \sigma_2}$$

where σ_1 and σ_2 are the standard deviations in the data points i through $(i+2)$, and $(i+4)$ through $(i+6)$, respectively. The test function now has the values (1, 1, 1, 0, −1, −1, −1). Again, the ten time points with the largest values of F are chosen.

Next, the ten likely single molecule events from both cross-correlation functions are compared to check for redundancy. After deleting any duplicate events, the two lists are combined into one final group of times at which single molecule dissociations occurred. The distribution of these times is then fitted with an exponential probability density function to find τ, the lifetime of the antibody–antigen bond:

$$f(t) = \frac{1}{\tau} \mathrm{e}^{-t/\tau}.$$

The unbinding rate is simply the inverse of the lifetime. Finally, the time data are sorted into a histogram (number of events versus time) which can be seen in figure 5. The events with the lowest values of CCF (i.e. the largest red-shifts) are collected in the same way, resulting in a histogram that reflects the random timing of these events.

The results of this analysis are plotted in figures 3(b)–(f). All of the blue-shifts from two experiments are plotted in figures 5(c) and (d). Note that the shift magnitude is greater for the experiment shown in (d), and that the data also have a higher noise level; this is due to slight variations in signal level and sensitivity among the individual bipyramids. The average blue-shift for all events was 0.34 nm. The probability distribution of single blue-shifts versus rinse time was fitted with an exponential distribution and the unbinding rate was found to be $7.9 \pm 1.3 \times 10^{-5}$ s^{-1}, in good agreement with ensemble measurements on the same antibody and molecular target [8, 9]. Finally, the blue-shifts collected from all experiments were combined, binned according to their rinse time, and plotted as a histogram in figure 5(e). As a control, the red-shifts were analysed in the same manner, and their histogram is plotted in figure 5(f). The histogram of red-shifts is featureless, indicating that these correspond to random fluctuations in the signal rather than a specific molecular process. The preponderance of discrete red-shifts is likely due to the gradual drift of the signal towards longer wavelengths upon the final rinse step (see figure 5(a)).

To investigate the magnitude of LSPR shift that should be expected, finite element method (FEM) simulations were carried out with parameters that precisely matched the experimental conditions. A gold bipyramid (140 nm × 50 nm, 5 nm tip radius) was simulated to be sitting on a glass substrate ($n = 1.5$) in water ($n = 1.33$). Capture antibodies absorbed to the bipyramid were represented by a

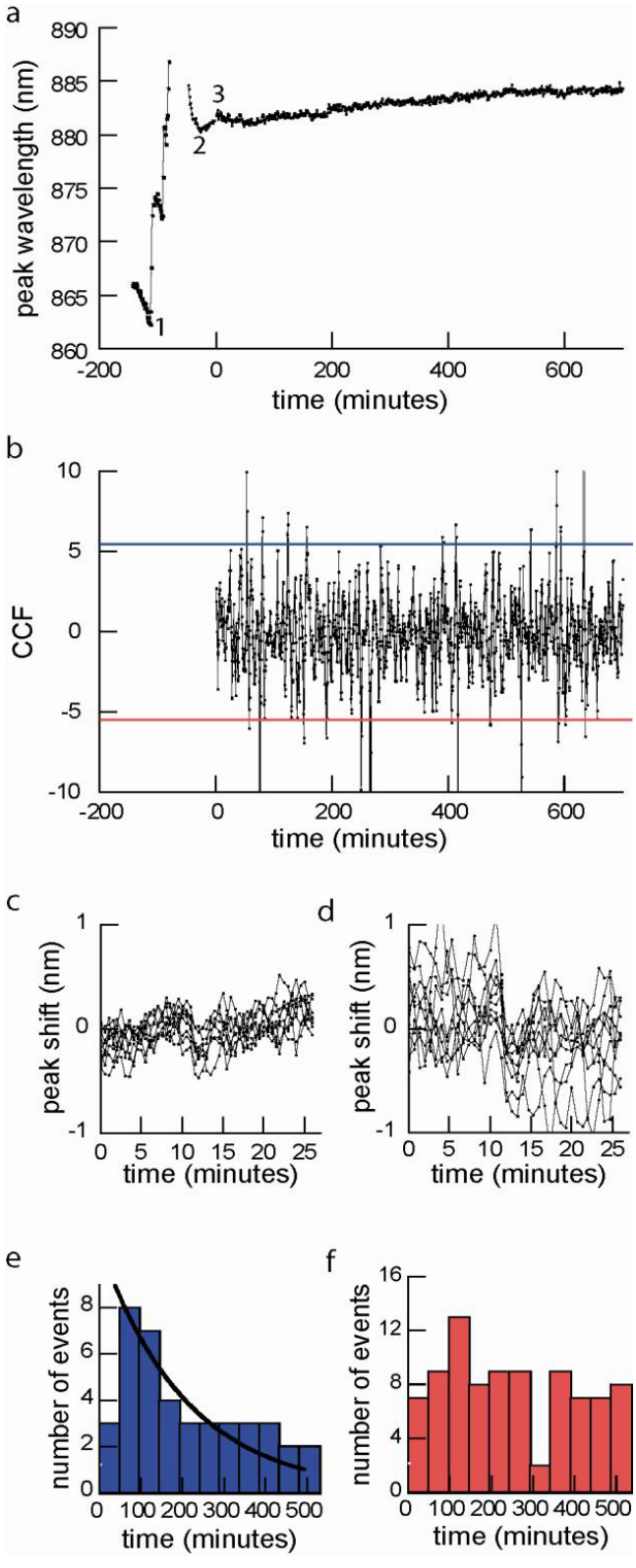

Figure 5. Single particle immunoassay data. (a) LSPR signal obtained from single particle spectra of a bipyramid in a flow cell, where it was exposed to (1) the capture antibody (Rabbit IgG), (2) the molecular target (Goat anti-Rabbit IgG), and (3) the PBS buffer rinse. (b) Cross-correlation function of the data with a step function. (c) and (d) Discrete blue-shifts (i.e. single molecule unbinding events) collected from two different experiments. (e) and (f) Histograms of all discrete blue- and red-shifts.

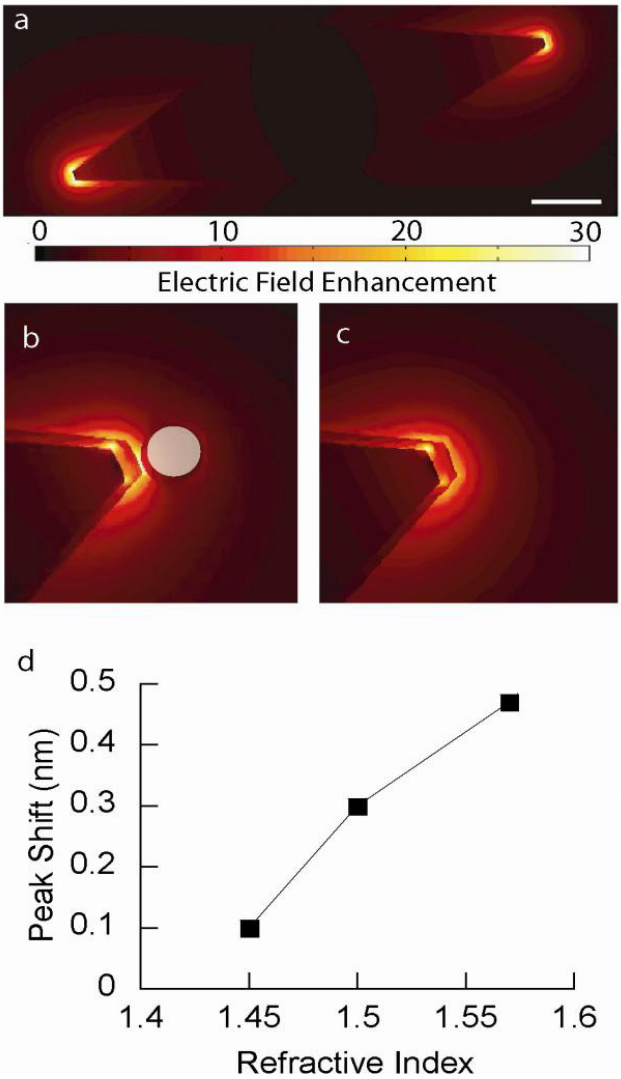

Figure 6. FEM simulations. (a) The electric field distribution around a gold bipyramid (scale bar is 20 nm). The local electric fields at the bipyramid tip (b) in the presence and (c) in the absence of a dielectric molecule. (d) The calculated spectral shift for molecules of differing refractive index.

5 nm dielectric film on the bipyramid. The film was assigned a refractive index of 1.57 to match previous determinations of the index of refraction of proteins [19]. The molecular target (secondary antibody) was simulated as a 7.1 nm diameter sphere, which was found by dividing its molecular weight by the average density of hydrated proteins [20]. The target was also given a dielectric constant of 1.57. Extinction spectra and maps of the local field intensity were calculated for the bipyramid both with and without the molecular target present at the tip. The field distribution around the bipyramid, displayed in figures 6(a)–(c), indicates the localization of the field enhancement around the tips. The calculated spectral extinction is comparable to the measured single bipyramid scattering spectra since the extinction for nanoparticles the size of these bipyramids is predominantly due to scattering. For the parameters given above, the spectral shift was found to be 0.45 nm, somewhat larger than our experimentally observed average shift of 0.34 nm. The protein dielectric constant

was then varied and the simulations repeated. As seen in figure 6(d), the experimental shift is reproduced at $n = 1.54$, which suggests that this is the effective index of the individual antibody molecules.

The LSPR detection method described here has several unique properties that could address unmet needs in single molecule research. Foremost is the 10^5 s timescale over which LSPR sensing can observe molecular interactions. Fluorescence-based measurements like single molecule Förster resonance energy transfer (FRET) [21] combined with sensitive imaging methods like confocal fluorescent microscopy [22] or total internal reflectance fluorescent microscopy (TIRFM) [23] have been used to investigate many biomolecular mechanisms. However, photobleaching limits the time scales that can be studied with these techniques to 10^2 s. Single molecule force spectroscopy by optical tweezers and AFM can elucidate complex molecular motions and energy landscapes, but is also limited to approximately 10^2 s due to mechanical stability and radiation damage [24]. Electrophysiological measurements of single ion channels are limited to a similar timescale due to the finite lifetime of the membrane–pipette seal [25].

Single molecule sensing by LSPR shifts also benefits from the non-invasive nature of the measurements. Since the target molecule's refractive index is detected, there is no need for chemical modification of the target or subsequent binding of other factors to it to generate a signal. Furthermore, the measurements are not taken under any applied load or tension, which are known to affect bond strengths in a load-rate dependent manner [26]. In single molecule LSPR experiments, the target molecule is only perturbed by the optical near-field of the nearby gold bipyramid [27].

The only other label-free, single molecule method previously reported was based on the effect of heat generated by optically irradiated biomolecules on a whispering gallery mode (WGM) resonator [28]. The WGM biosensor achieved a higher signal to noise ratio due to single molecule binding/unbinding, but this is not surprising since the WGM resonator exhibits a much higher quality factor than nanoparticle LSPR. However, the LSPR sensor has the advantage that it does not require microfabrication and can be monitored by simple far field optics. In fact, the bipyramid substrates described here were fabricated entirely by chemical synthesis and self-assembly. This ultimate limit of detection achieved by WGM and now LSPR sensors could have significant impact in several biomedical areas including proteomics, point-of-care diagnostics, and drug discovery [1, 29].

In summary, due to their sharp tips, and bright, sharp spectral scattering resonances, gold bipyramids are well suited for LSPR biosensing. The high sensitivity of the bipyramids allowed single molecule antibody–antigen dissociation events to be observed with no labels and in real time. Analysis of the times at which these events occurred yielded an antibody–antigen unbinding rate of $7.9 \pm 1.3 \times 10^{-5}$ s^{-1}, consistent with the kinetic rate measured for an ensemble sample [8]. This is the first measurement of the kinetics of a biomolecular bond by a label-free, single molecule method and shows that LSPR sensing with simple optics and chemically synthesized nanoparticles holds great promise as a biological sensing technology at the single molecule level.

Acknowledgments

KM acknowledges support from the NSF funded Integrative Graduate Research and Educational Training (IGERT) program (DG0504425) in nanophotonics. This work was also supported by the National Science Foundation's Nanoscale Science and Engineering Initiative under award no. EEC-0647452, the US Army Research Office under grant no. W911NF-04-1-0203, and the Welch Foundation under grants C-1556 and C-1222

References

[1] Anker J N, Hall W P, Lyandres O, Shah N C, Zhao J and Van Duyne R P 2008 Biosensing with plasmonic nanosensors *Nat. Mater.* **7** 442–53
[2] Haes A J, Stuart D A, Nie S M and Van Duyne R P 2004 Using solution-phase nanoparticles, surface-confined nanoparticle arrays and single nanoparticles as biological sensing platforms *J. Fluorescence* **14** 355–67
[3] Unger A, Rietzler U, Berger R and Kreiter M 2009 Sensitivity of crescent-shaped metal nanoparticles to attachment of dielectric colloids *Nano Lett.* **9** 2311–5
[4] Larsson E M, Alegret J, Kall M and Sutherland D S 2007 Sensing characteristics of NIR localized surface plasmon resonances in gold nanorings for application as ultrasensitive biosensors *Nano Lett.* **7** 1256–63
[5] Nehl C L, Liao H W and Hafner J H 2006 Optical properties of star-shaped gold nanoparticles *Nano Lett.* **6** 683–8
[6] Hao F, Nehl C L, Hafner J H and Nordlander P 2007 Plasmon resonances of a gold nanostar *Nano Lett.* **7** 729–32
[7] Liu M and Guyot-Sionnest P 2005 Mechanism of silver(I)-assisted growth of gold nanorods and bipyramids *J. Phys. Chem.* B **109** 22192–200
[8] Mayer K M, Lee S, Liao H, Rostro B C, Fuentes A, Scully P T, Nehl C L and Hafner J H 2008 A label-free immunoassay based upon localized surface plasmon resonance of gold nanorods *ACS Nano* **2** 687–92
[9] Lee S, Mayer K M and Hafner J H 2009 Improved localized surface plasmon resonance immunoassay with gold bipyramid substrates *Anal. Chem.* **81** 4450–5
[10] Burgin J, Liu M Z and Guyot-Sionnest P 2008 Dielectric sensing with deposited gold bipyramids *J. Phys. Chem.* C **112** 19279–82
[11] Sönnichsen C, Franzl T, Wilk T, von Plessen G and Feldmann J 2002 Drastic reduction of plasmon damping in gold nanorods *Phys. Rev. Lett.* **88** 077402
[12] Raschke G *et al* 2004 Gold nanoshells improve single nanoparticle molecular sensors *Nano Lett.* **4** 1853–7
[13] Sherry L J, Chang S-H, Schatz G C and Van Duyne R P 2005 Localized surface plasmon resonance spectroscopy of single silver nanocubes *Nano Lett.* **5** 2034–8
[14] Rindzevicius T, Alaverdyan Y, Dahlin A, Hook F, Sutherland D S and Kall M 2005 Plasmonic sensing characteristics of single nanometric holes *Nano Lett.* **5** 2335–9
[15] Sherry L J, Jin R, Mirkin C A, Schatz G C and Van Duyne R P 2006 Localized surface plasmon resonance spectroscopy of single silver triangular nanoprisms *Nano Lett.* **6** 2060–5
[16] Baciu C L, Becker J, Janshoff A and Sonnichsen C 2008 Protein–membrane interaction probed by single plasmonic nanoparticles *Nano Lett.* **8** 1724–8

[17] Unger A, Rietzler U, Rudiger B and Kreiter M 2009 Sensitivity of crescent-shaped metal: nanoparticles to attachment of dielectric colloids *Nano Lett.* **9** 2311–5
[18] Bukasov R and Shumaker-Parry J S 2007 Highly tunable infrared extinction properties of gold nanocrescents *Nano Lett.* **7** 1113–8
[19] Jung L S, Campbell C T, Chinowsky T M, Mar M N and Yee S S 1998 Quantitative interpretation of the response of surface plasmon resonance sensors to adsorbed films *Langmuir* **14** 5636–48
[20] Squire P G and Himmel M E 1979 Hydrodynamics and protein hydration *Arch. Biochem. Biophys.* **196** 165–77
[21] Webb S E D, Roberts S K, Needham S R, Tynan C J, Rolfe D J, Winn M D, Clarke D T, Barraclough R and Martin-Fernandez M L 2008 Single-molecule imaging and fluorescence lifetime imaging microscopy show different structures for high- and low-affinity epidermal growth factor receptors in A431 cells *Biophys. J.* **94** 803–19
[22] Shi J, Dertouzos J, Gafni A, Steel D and Palfey B A 2006 Single-molecule kinetics reveals signatures of half-sites reactivity in dihydroorotate dehydrogenase A catalysis *Proc. Natl Acad. Sci. USA* **103** 5775–80
[23] Kuhn J R and Pollard T D 2007 Single molecule kinetic analysis of actin filament capping-polyphosphoinositides do not dissociate capping proteins *J. Biol. Chem.* **282** 28014–24
[24] Neuman K C and Nagy A 2008 Single-molecule force spectroscopy: optical tweezers, magnetic tweezers and atomic force microscopy *Nat. Methods* **5** 491–505
[25] Knight A E 2009 *Single Molecule Biology* (Amsterdam: Elsevier) p 332
[26] Merkel R, Nassoy P, Leung A, Ritchie K and Evans E 1999 Energy landscapes of receptor–ligand bonds explored with dynamic force spectroscopy *Nature* **397** 50–53
[27] Liu M Z, Guyot-Sionnest P, Lee T W and Gray S K 2007 Optical properties of rodlike and bipyramidal gold nanoparticles from three-dimensional computations *Phys. Rev.* B **76** 235428
[28] Armani A M, Kulkarni R P, Fraser S E, Flagan R C and Vahala K J 2007 Label-free, single-molecule detection with optical microcavities *Science* **317** 783–7
[29] Arnold S, Keng D, Shopova S I, Holler S, Zurawsky W and Vollmer F 2009 Whispering gallery mode carousel–a photonic mechanism for enhanced nanoparticle detection in biosensing *Opt. Express* **17** 6230–8